Journal of Structural Biology 171 (2010) 1–10

Contents lists available at ScienceDirect

Journal of Structural Biology

journal homepage: www.elsevier.com/locate/yjsbi

Solution structures of 2 × 6-meric and 4 × 6-meric hemocyanins of crustaceans *Carcinus aestuarii*, *Squilla mantis* and *Upogebia pusilla*

Ivan Mičetić [a], Carmen Losasso [b], Paolo Di Muro [a], Giuseppe Tognon [c], Piero Benedetti [a], Mariano Beltramini [a,*]

[a] Department of Biology, University of Padova, via Ugo Bassi 58/B, I-35131 Padova, Italy
[b] Department of Onco-Hematology, IRCCS-Oncology Referral Center of Basilicata, via Padre Pio 1, I-85028 Rionero in Vulture (Pz), Italy
[c] CNR Institute of Biomedical Technologies, University of Padova, via Ugo Bassi 58/B, I-35131 Padova, Italy

ARTICLE INFO

Article history:
Received 5 November 2009
Received in revised form 10 March 2010
Accepted 23 March 2010
Available online 27 March 2010

Keywords:
Quaternary structure
Hemocyanin
Solution scattering
Oligomeric proteins

ABSTRACT

Arthropod hemocyanins (Hcs) are a family of large, high molecular mass, extracellular oxygen transport proteins. They form oligomeric quaternary structures based on different arrangements of a basic 6 × 75 kDa hexameric unit. Their complex quaternary structures present binding sites for allosteric effectors and regulate the oxygen binding process in a cooperative manner. In order to describe the functional regulation of arthropod Hcs, a detailed description of their quaternary structure is necessary. We have utilized small angle X-ray scattering to characterize the structure of three arthropod Hcs in unperturbed conditions. Two different levels of complexity are evaluated: for the 2 × 6-meric case, we analyzed the Hcs of the portunid crab *Carcinus aestuarii* and stomatopod *Squilla mantis*, while in the case of 4 × 6-meric structures, we studied the Hc of the thalassinid shrimp *Upogebia pusilla*. While *C. aestuarii* Hc presented a structure comparable to other 2 × 6-meric crustacean Hcs, *S. mantis* Hc shows a peculiar and quite unique arrangement of its building blocks, resembling a substructure of giant Hcs found among cheliceratans. For *U. pusilla*, the arrangement of its subunits is described as tetrahedral, in contrast to the more common square planar 4 × 6-meric structure found in other arthropod Hcs.

1. Introduction

The biological role of Hemocyanins (Hcs), a family of oxygen transport proteins present in the hemolymph of most arthropods and molluscs, is based on the reversible binding of molecular oxygen to a binuclear copper active site (Markl and Decker, 1992; Salvato and Beltramini, 1990). These proteins are characterized by a complex quaternary structure that provides the structural basis for the onset of the allosteric behavior exhibited by the oligomers (van Heel and Dube, 1994).

In arthropods, the reference structures are hexameric proteins (1 × 6-mer) isolated from the lobster *Panulirus interruptus* and the horseshoe crab *Limulus polyphemus* (subunit II). Such structures have been solved by crystallographic methods allowing for a precise definition of the inter-subunits interactions within the hexamer (Volbeda and Hol, 1989; Hazes et al., 1993). Hc hexamers are organized as a two-layer aggregate where each layer includes three subunits, shifted 30° with respect to each other. A threefold symmetry axis connects the subunits along the axial position of the molecule, whereas three twofold symmetry axes, running perpendicular to the threefold axis, connect the subunits belonging to different layers (D_3 point-group symmetry). Arthropod Hcs subunits are made by a polypeptide chain folded as to form a three-domain structure of ~75 kDa.

The active site, formed by domain two, is deeply buried in the protein matrix where six histidine residues, belonging to a four antiparallel α-helical motif, represent the ligands for two copper ions that are fundamental for dioxygen binding. The availability of several subunits sequences (Burmester, 2002), of crystallographic structure of two deoxy-Hcs (*P. interruptus* a and b subunits (Volbeda and Hol, 1989), *L. polyphemus* subunit II (Hazes et al., 1993)), one oxy-Hc (*L. polyphemus* subunit II (Magnus et al., 1994)) and of the homolog prophenoloxidase from *Manduca sexta* (Li et al., 2009), have provided important hints to address some fundamental questions on Hc molecular physiology such as the structural basis for the oligomerization and the structural changes occurring upon binding of dioxygen.

Hcs are widely distributed within arthropods and there is not a unique quaternary structure within the *taxon*. In addition to the 1 × 6-mer, the oligomerization state of the arthropod Hcs includes 2 × 6, 4 × 6, 6 × 6 and 8 × 6-meric depending on the species (Markl and Decker, 1992; Salvato and Beltramini,

* Corresponding author. Fax: +39 0498276300.
E-mail address: mariano.beltramini@unipd.it (M. Beltramini).

1047-8477/$ - see front matter © 2010 Elsevier Inc. All rights reserved.
doi:10.1016/j.jsb.2010.03.012

1990). The molecular complexity increases, due to the increase of heterogeneity in subunit composition of the aggregates, where specific subunits play a key role in the quaternary structure organization (Voit et al., 2000; Bruneaux et al., 2009; Kusche et al., 2003; Decker et al., 1989). In most cases we are currently not able to predictively describe the oligomeric assembly starting from basic hexameric units.

Several studies aimed at a thorough description of the hierarchical aggregation of such giant molecules exploited non-crystallographic approaches such as conventional electron microscopy (EM) and cryo-electron microscopy (cryo-EM), and small angle X-ray scattering (SAXS). With these approaches, the quaternary structures of the 1×6-meric Hc from lobsters *Palinurus elephas* (by cryo-EM, Meissner et al., 2003) and *Homarus americanus* (by SAXS, Hartmann et al., 2001), horseshoe crab *L. polyphemus*, centipede *Scutigera coleoptrata* and scorpion *Pandinus imperator* (by cryo-EM, Taveau et al., 1997; Martin and et al., 2007; Markl et al., 2009; Cong and et al., 2009) and the tarantula *Eurypelma californicum* (by SAXS and EM, Hartmann and Decker, 2002; Decker et al., 1996; De Haas and van Bruggen, 1994) have been solved to a resolution as good as ~20–30 Å in case of SAXS and ~7 Å in case of cryo-EM.

In this paper we have studied by SAXS the quaternary organization of three Hcs characterized by two levels of complexity: the 2×6-meric and the 4×6-meric. In the former case, two proteins have been considered: the Hc of the portunid crab *Carcinus aestuarii* and that of the stomatopod *Squilla mantis*. Based on previous EM studies (Markl and Decker, 1992; Bijlholt and van Bruggen, 1986) they differ in the quaternary organization and our intention was to characterize by SAXS their structures at a higher resolution. In particular, since previous EM studies proposed two possible models for *S. mantis* Hc we have used SAXS to verify and validate them. As far as the 4×6-meric level of organization is concerned, we present here the description of the Hc isolated from the thalassinid shrimp *Upogebia pusilla*. Based on a conventional EM study, thalassinid 4×6-meric Hcs have a quaternary structure completely different from the aggregation state exhibited by 4×6-meric cheliceratan Hcs (Cavellec et al., 1989). In this particular case we have described the structure of the oligomer and its symmetry.

2. Materials and methods

2.1. Protein purification

The Hcs of the present study were purified from the hemolymph of living specimens by standard procedures: (Bubacco et al., 1992) for *C. aestuarii* and *S. mantis* Hc and (Paoli et al., 2007) for *U. pusilla* Hc. The proteins were purified to high concentrations (>25 g l^{-1}) in 50 mM Tris/HCl, 20 mM $CaCl_2$, pH 7.6 and stored with 20% sucrose as a cryoprotectant at −20 °C. The Hc concentration was determined spectrophotometrically using an extinction coefficients $\varepsilon_{280} = 1.21$ ml mg^{-1} cm^{-1} for *C. aestuarii* and *S. mantis* Hc or $\varepsilon_{280} = 1.11$ ml mg^{-1} cm^{-1} for *U. pusilla* Hc. The quality of Hc preparations was checked from the absorbance ratio A_{337}/A_{278} assuming a value 0.21 or better for a solution of fully oxygenated protein.

2.2. Sample preparation and SAXS measurements

Prior to SAXS measurements, sucrose was eliminated from native protein stocks by an overnight dialysis against 50 mM Tris/HCl, 20 mM $CaCl_2$, pH 7.6. Homogeneous solutions of the oligomers under study were obtained by eluting the whole Hc solutions in size exclusion chromatography on a Pharmacia FPLC system (SEC-FPLC) using a prep-grade Hi-Load Superdex 200 26/60 column or a Sephacryl S-300 XK 26/60 column (Pharmacia). The higher retention time material corresponding to the 2×6-meric (in the case of *C. aestuarii* and *S. mantis* Hc) or 4×6-meric (in the case of *U. pusilla* Hc) fraction was collected and concentrated. The stability of each oligomer was checked by a second chromatography of the pooled material. All protein samples were fully oxygenated and diluted in the above buffer to the final concentration of 4 g l^{-1}.

Small angle scattering measurements were performed at the European Synchrotron Radiation Facility (Grenoble, France). Measurements were carried out under standard experimental setup at the public beamline ID2 (high brilliance). The wavelength of the monochromatic $\Delta\lambda/\lambda = 10^{-4}$ X-ray beam was 0.995 Å (at $E = 12.4$ keV). The scattering pattern was recorded on 2D, ESRF developed FReLoN CCD camera coupled to a Thomson X-ray image intensifier (XRII) at the resolution of 1024×1024 (binned mode) (Narayanan et al., 2001). The sample-detector distance was set to 2 m giving a scattering vector q in the range 0.04–2.31 nm^{-1} where $q = 4\pi \sin(\theta)/\lambda$ and 2λ is the scattering angle. Several protein concentrations were tried in order to minimize interparticle interactions and maximize the signal-to-noise ratio. At the used concentration of 4 g l^{-1}, no particle interactions were observed. The samples were measured in quartz capillaries (diameter 1 mm) at room temperature. Data reduction was performed using in-house programs and involved flux, detector response, exposure time and sample transmission normalization. Multiple 0.5 s exposures of protein samples with relative buffers were averaged and subsequently subtracted. Experimental curves at the beginning and at the end of the experiment were superimposable with used exposure times so no radiation damage effects could be observed.

2.3. SAXS data analysis and modeling strategy

The radius of gyration (R_g), pair distribution function $p(r)$, the estimation of maximum particle dimension (D_{max}) and the preparation of the scattering curve for successive modeling steps were performed by the indirect transform program GNOM (Svergun, 1992; Svergun et al., 1988) (Fig. 1). Theoretical scattering patterns were calculated from atomic coordinates up to an angle of 0.25 $Å^{-1}$ using CRYSOL (Svergun et al., 1995) with 15 orders of spherical harmonics expansion and default solvent and protein electron densities. During the modeling process, a 3.2 Å crystal structure of deoxy-hexameric *Panulirus interruptus* Hc (Protein Data Bank accession number 1HCY) was used since it represents the only crustacean Hc structure known at high resolution (Volbeda and Hol, 1989).

Ab initio structures of oligomeric proteins were modeled with the use of SASREF, a rigid body multi-subunit modeling program (Petoukhov and Svergun, 2005). The alignment, comparison and averaging of multiple structural models was done using DAMAVER software package (Kozin and Svergun, 2001; Volkov and Svergun, 2003). DAMAVER processing of structural models produces a lower resolution, dummy atom (DA) bead model as a representative average structure. DA bead models were transformed to a volumetric map by the convolution of the DA lattice with a Gaussian kernel with the use of PDB2VOL utility from the SITUS program package (Wriggers and Chacon, 2001).

The quality of the obtained structural models was assessed from the χ^2 merit function between experimental and calculated SAXS profiles defined as:

$$\chi^2 = \frac{1}{N-1}\sum_i \left[\frac{I_{exp}(q_i) - cI(q_i)}{\sigma(q_i)}\right]^2$$

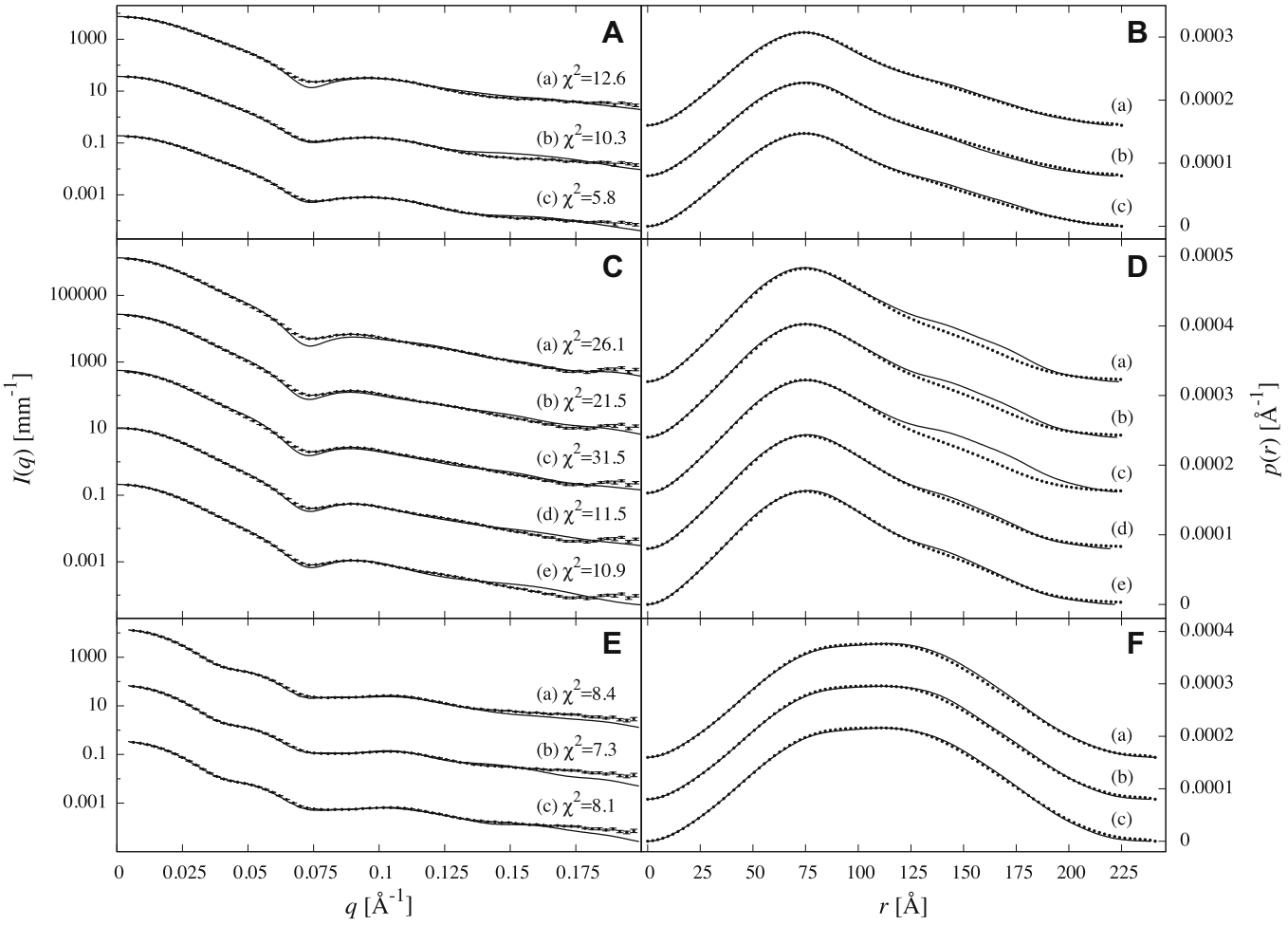

Fig. 1. Experimental and theoretical SAXS patterns and corresponding $p(r)$ functions of three crustacean hemocyanins. Left column shows SAXS patterns while right column shows corresponding $p(r)$ functions. Experimental curves are shown as points overlaid with modeled ones shown as solid lines. The goodness-of-fit value χ^2 is shown for every modeled structure. Every fourth experimental data point is plotted and all curves are displaced along the y-axis for clarity. (A and B) *C. aestuarii* modeling: SAXS patterns of starting models of *E. californicum* 2 × 6-meric and *C. pagurus* Hc used for the fits are shown in (a) and (b), respectively, while the final, best-fit model of *C. aestuarii* Hc is shown in (c). (C and D) *S. mantis* modeling: SAXS patterns of starting models of *S. mantis* EM model I, III and *P. imperator* 2 × 6-meric Hc used for the fits are shown in (a–c), respectively. Curve (d) shows the SAXS pattern of optimized EM models, while the final, best-fit model of *S. mantis* Hc is shown in (e). (E and F) *U. pusilla* modeling: SAXS patterns of the three SAXS best-fit models (1, 2 and 3) are shown in curves (a–c), respectively.

where N is the number of experimental points, c is a scaling factor and $\sigma(q_i)$ is the experimental error at the momentum transfer q_i (Petoukhov and Svergun, 2005).

2.4. Electron microscopy and image analysis

Samples were prepared as suggested by Ohi et al. (2004). A 5 µl drop of sample solution was adsorbed to a glow-discharged carbon-coated copper grid, washed with two drops of deionized water, and stained with two drops of freshly prepared 0.75% uranyl acetate. Samples were imaged at room temperature using a Fei Tecnai T12 electron microscope equipped with a LaB_6 filament and operated at an acceleration voltage of 100 kV. Images were taken at a calibrated magnification of 36,000×.

Hc particles were manually picked from electron micrographs with the module Boxer of the EMAN software package (Ludtke et al., 1999). A total of 370 particles were selected in 128 × 128 boxes with a pixel size of 3.65 Å. The following particle analysis was carried out with SPIDER image processing package (Frank et al., 1996). Selected particles were band-pass filtered at 25 and 250 Å, normalized for intensity and circularly masked with a Gaussian falloff function. Multi-reference alignment of the particles was done against low-pass filtered volume projections of protein models obtained from SAXS data. Cross correlation was used as a similarity measure between boxed particles and simulated 2D projections of SAXS derived models.

3. Results

The 1 × 6-meric is the only quaternary structure of arthropod Hc known at crystallographic resolution. This limitation imposes a strategy to build up starting models, which involves the use of crystallographic coordinates for hexamer modeling and information on inter-hexameric arrangement based on available non-crystallographic methods (Hartmann and Decker, 2004). Thus, 2 × 6-meric structures were generated by the arrangement of two *P. interruptus* hexamers. Moving the hexameric building blocks according to different strategies and minimizing the discrepancies between the experimental and modeled SAXS curve refined these initial models. Experimental SAXS patterns of different Hcs are shown in Fig. 1A, C, and E and compared with curves resulting from different models. Fig. 1B, D and F shows the corresponding $p(r)$ functions calculated from SAXS data. For each modeled case, the experimental SAXS data and the corresponding $p(r)$ functions are reported for every fit in order to bet-

ter visualize the correspondence between experimental and model-based theoretical curves. Reduced residual plots of all fits are shown in Supplementary Fig 1.

3.1. C. aestuarii hemocyanin modeling

Measured SAXS pattern of *C. aestuarii* Hc is shown in Fig. 1A and B and the obtained invariants radius of gyration (R_g) and maximum particle length (D_{max}) are reported in Table 1. R_g and D_{max} are 72 ± 1 and 225 ± 5 Å, respectively, in very good agreement with those reported for the 2 × 6-meric Hc from *H. americanus* (72.1 ± 0.05 and 235 Å, respectively (Hartmann et al., 2001). The molecular mass determined from the forward scattering intensity is in agreement with the 2 × 6-meric state of this Hc species (Table 1).

SAXS refinement of a structural model derived by negative-stain EM was successfully applied by Hartmann et al. (2001) in the case of *H. americanus*. Therefore we have used a similar approach using as starting models two structures for decapod 2 × 6-meric Hcs available in literature. The first one is the Hc of *C. pagurus* described by De Haas et al. (1991) from negative-stain EM images and successively refined by Hartmann et al. (2001). The second one is represented by *E. californicum* Hc. This Hc in native state is a 4 × 6-mer, formed by two-staggered 2 × 6-mers that have been described by Hartmann and Decker (2002) using SAXS. CRYSOL program was used to calculate the scattering curve from the models and compare them to the experimental curve giving χ^2 values of 10.3 and 12.6. The comparison of experimental SAXS curve of *C. aestuarii* Hc with the curves generated from the two available models is shown in Fig. 1A and B.

In order to obtain the best representation of *C. aestuarii* Hc structure, we have used both available 2 × 6-meric structures as starting models (called a and b) (Fig. 2A and B). For the first starting model, a *P. interruptus* hexameric structure was oriented so that its threefold symmetry axis coincides with the *z*-axis pointing to the observer while the *x*-axis coincides with one of the twofold axes as described by De Haas and van Bruggen (1994). In order to accommodate the second hexamer, the hexamer with the orientation described above was shifted by a vector (−117.5, −0.05, 0.00) and held fixed during the fitting procedure (lower hexamer). The position of the upper hexamer was obtained from 30 runs of SASREF program. Initially, a coarse 5 Å translational and 20° angular step size was used. The structures obtained were clustered according to the χ^2 value and the positional vector of the upper hexamer. In this way it was possible to choose a typical, most representative best-fit structure. Such structure was used as a starting point for another 30 runs of SASREF, this time with much finer sampling steps (1 Å translational and 5 degrees rotational step). By this procedure we have adjusted the position of the two hexamers and obtained a model that gives the lowest χ^2 value. Both initial models, a and b, converged to the same final model shown in Fig. 2C, with the χ^2 value of 5.8. Its scattering curve compared to the experimental one shown in Fig. 1A and the corresponding pair distribution function calculated from the atomic model is shown in Fig. 1B. Reduced residuals for both functions are shown in Supplementary Fig. 1A and B. Model scattering curve is consistent with the experimental one with deviations around a first minimum and at high angles. Increased minimum in the modeled structure is an indication of a more spherical structure while deviations at high angles (bringing high-resolution information) are attributed to the use of a non-native hexameric structural unit for modeling purposes. Calculated $p(r)$ function follows closely the experimental one with deviations around 150 Å showing increased inter-hexameric distances with respect to experimental data and therefore resulting in a slightly more compact model. However, increasing the inter-hexameric distance in the final model was not enough to further improve the presented model. Table 2 reports Euler angles and translational vector of the representative, best-fit model.

Table 1
SAXS invariants of three different hemocyanins. For experimental conditions see Section 2.

	R_g [Å][a]	D_{max} [Å][b]	$I(0)/c$ [ml mg^{-1} mm^{-1}][c]	M_r[c]
C. aestuarii	72 ± 1	225 ± 5	0.047 ± 0.002	818, 000
S. mantis	72 ± 1	234 ± 5	0.052 ± 0.003	910, 000
U. pusilla	84 ± 1	241 ± 5	0.088 ± 0.004	1532, 000

[a] Indirect transform program GNOM underestimates the error of the radius of gyration so a reasonable estimate is shown instead.
[b] Maximum particle dimension has no associated error value, as obtained from GNOM, but is estimated to be around 5 Å.
[c] Molecular mass calculations obtained from the scattering intensity at zero angles are sensitive to the protein concentration, which has a typical error of 5–10%. Therefore SAXS determined molecular masses of proteins are accurate to within 10%.

3.2. S. mantis hemocyanin modeling

The values of R_g and D_{max} obtained for this Hc are similar to those obtained for *C. aestuarii* with *S. mantis* Hc being a bit larger. Again the molecular mass determined from the forward scattering intensity is in agreement with the 2 × 6-meric state of this Hc species (Table 1). The scattering patterns and $p(r)$ functions are shown in Fig. 1C and D, respectively.

A two step process was used to model *S. mantis* Hc: refinement of the structure constructed following Bijlholt and van Bruggen (1986), who proposed a structural model from negative-stain EM observations, followed by a full six-dimensional rigid body search procedure.

In the first step, two all-atoms structural models were built according to negative-stain EM study namely model I and model III according to Bijlholt and van Bruggen (1986). The two models differ for the mutual rotation of the stacked hexamers; in model I, the hexamers are in contact through one subunit while in model III two subunits from each hexamer are involved in contact as shown in Fig. 3. As in the case for *C. aestuarii*, *P. interruptus* structure was used for modeling purposes. The comparisons of calculated and experimental scattering curves are shown in Fig. 1C. The EM-based models (models I and III) give remarkably high χ^2 (Fig. 1C, curves a and b, with χ^2 of 26.1 and 21.6, respectively).

To improve the model, the position of the upper hexamer was optimized to the SAXS pattern by performing a full 3D translational search procedure. At every step of a procedure, the upper hexamer was shifted ±60 Å in all directions at steps of 6 Å creating C^{α} atom models for both model I and model III. Successively, CRYSOL program was used to calculate the scattering curves from the models and compare them to the experimental one. From such best-fit structures, another round of 3D search procedure with step size of 1 Å using all-atom models was executed. Both starting models converged to the same optimized model lowering the χ^2 to 13.4.

To further improve the *S. mantis* Hc structural model, it was necessary to enable the free rotation of the upper hexamer. Therefore, as a second step, a 6-parameter rigid body modeling of *S. mantis* Hc was accomplished with 30 runs of SASREF program with coarse translational and rotational step sizes (1 Å and 5°) followed by another 30 rounds with finer parameter space sampling (0.5 Å and 2°). A representative best-fit structure is presented in Fig. 3D with corresponding fits and pair distribution functions (Fig. 1C, D, curve d). In this way it was possible to decrease slightly the χ^2 value to 11.5.

Upon inspection of the modeled structure of *S. mantis* Hc, we have found that it resembles closely a substructure of larger cheliceratan 4 × 6-meric and 8 × 6-meric Hcs (Martin and et al., 2007;

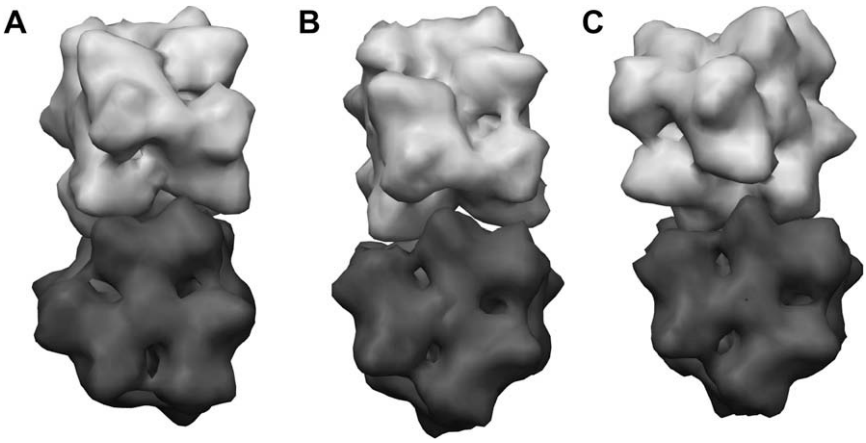

Fig. 2. Starting and final models of *C. aestuarii* Hc. Structures of starting models utilized for *C. aestuarii* Hc modeling: *E. californicum* 2 × 6-meric Hc (Hartmann and Decker, 2002) (A) and *C. pagurus* Hc (Hartmann et al., 2001) (B). Structure of the final, best-fit model of *C. aestuarii* Hc is shown in (C).

Table 2
Best-fit model parameters of three arthropod hemocyanins as determined from SAXS data.

		Translational vector [Å][a]			Rotation by Euler angles [°][a]			χ^2
C. aestuarii	Upper hexamer	50.66	10.64	26.65	83.27	124.69	278.89	5.8
	Lower hexamer	−51.50	−0.15	0.00	0.00	0.00	0.00	
S. mantis	Upper hexamer	42.25	−34.85	2.60	183.31	98.47	330.30	10.9
	Lower hexamer	−34.03	34.06	−0.59	2.67	86.39	309.93	
U. pusilla model 1		50.29	30.59	34.68	213.50	49.44	115.65	8.4
U. pusilla model 2		49.94	31.10	36.01	270.06	78.70	63.73	7.3
U. pusilla model 3		49.37	40.68	26.98	308.10	12.17	12.62	8.1

[a] Rotational and translational parameters are given with high precision in order to accurately reproduce the modeled structures. However, the errors on structural parameters for the models are limited by the size of sampling steps utilized in fitting procedures which are 1 Å and 5° for *C. aestuarii*, 0.5 Å and 2° for *S. mantis* and 5 Å and 20° for *U. pusilla* models.

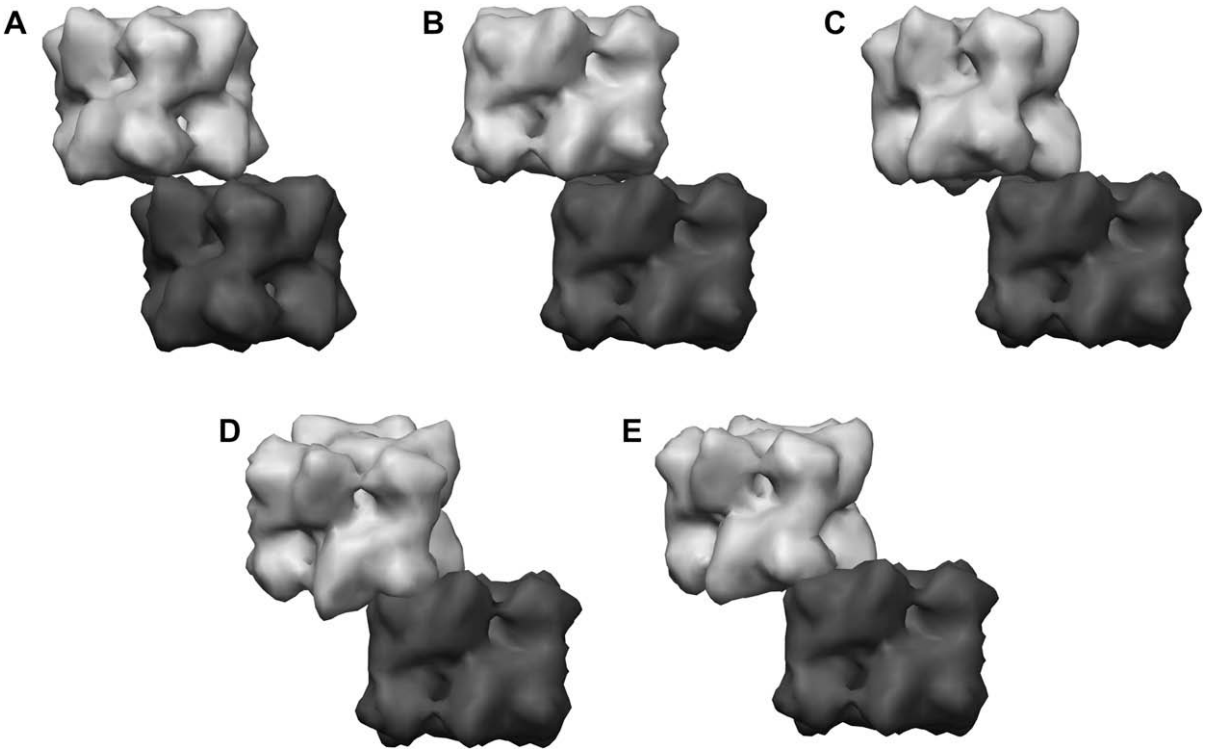

Fig. 3. Starting and final models of *S. mantis* Hc. Structures of starting models utilized for *S. mantis* Hc modeling: *S. mantis* EM model I (A), III (B) and *P. imperator* 2 × 6-meric Hc (C). Structure of the optimized EM-derived model is shown in (D), while the final, best-fit model of *S. mantis* Hc is shown in (E).

Cong and et al., 2009). Namely, in 4 × 6-meric and higher Hcs, two hexamers tightly assemble to form a 2 × 6-mer (called a dodecamer). Two identical dodecamers further dimerize in an antiparallel orientation producing a 4 × 6-meric Hc. *S. mantis* Hc bears a resemblance to a cheliceratan 2 × 6-meric obtained from two hexamers belonging each to a separate dodecamer. This lead to the generation of another starting model, utilizing the electron density map of resting state *P. imperator* Hc (Cong and et al., 2009) (Fig. 3C). Calculated SAXS pattern showed large differences with respect to the experimental *S. mantis* pattern giving a χ^2 value of 31.5. After two rounds of SASREF rigid body modeling with final step sizes of 0.5 Å and 2°, it was possible to obtain a better model for *S. mantis* Hc than starting from previously described EM-based models (Fig. 3E). Table 2 reports Euler angles and translational vector of this final best-fit model.

3.2. U. pusilla hemocyanin modeling

The R_g, D_{max} and M_r values obtained with *U. pusilla* Hc, shown in Table 1, are in agreement with the 4 × 6-meric state of this Hc (Paoli et al., 2007). The $I(0)$ intensity, and therefore molecular mass, invariant with respect to the shape of the particle, is roughly twice as large as both *C. aestuarii* and *S. mantis*. The R_g and D_{max} are in agreement with a different structure for *U. pusilla* with respect to cheliceratan Hcs. The 4 × 6-meric structure of thalassinid Hcs is peculiar among Arthropod Hcs since it shows a roughly tetrahedral packing of the four hexameric building blocks (Markl and Decker, 1992; Cavellec et al., 1989; Paoli et al., 2007), in contrast to a square planar arrangement of *E. californicum* and *P. imperator* 4 × 6-meric and *L. polyphemus* half molecules (van Heel and Dube, 1994; Taveau et al., 1997; Martin and et al., 2007; Cong and et al., 2009; Decker et al., 1996; De Haas and van Bruggen, 1994; De Haas et al., 1991; Bijlholt et al., 1982). The tetrahedral arrangement of hexameric building blocks results in a more compact structure characterized by a smaller R_g (84 ± 1 for *U. pusilla* against 88.0 ± 0.5 Å for *E. californicum*) and D_{max} (241 ± 5 for *U. pusilla* against 270 Å for *E. californicum*) (Hartmann and Decker, 2002).

Currently, from published EM-derived data, it is unknown if the four hexamers in *U. pusilla* Hc are arranged in a symmetrical or asymmetric manner. With that restriction in mind, we have modeled *U. pusilla* Hc assuming it to be a completely asymmetrical particle (C_1) or having D_2 symmetry. The modeling involved calculation of *ab initio* structures with SASREF program by imposing a *P*1 or *P*222 symmetry. A total of 40 and 30 runs of SASREF were executed in the case of symmetrical and asymmetrical particles, using 5 Å translational and 20° rotational step sizes. The asymmetrical models produced by SASREF were heterogeneous in subunit rotations while their reciprocal positions were more consistent. On the other hand, D_2 models converged to three structural solutions with similar χ^2 values (7.3–8.4). Representative structures of the three, symmetry imposed, structural solutions are shown in Fig. 4A–C with corresponding fits and pair distribution functions in Fig. 1E and F. The discrepancies between modeled and measured $p(r)$ functions for the three models show consistently an increase of the experimental curve around 75 Å and a decrease around 150 Å (Supplementary Fig. 1). As in the case of *C. aestuarii* Hc model, the three *U. pusilla* models are therefore slightly more compact than the native protein. The $p(r)$ region from 50 to 100 Å is determined by the shape of the *P. interruptus* hexamer used for modeling which proves to be less adequate to represent *U. pusilla* Hc while being acceptable for *C. aestuarii* and *S. mantis* Hcs.

All 40 symmetrical and 30 asymmetrical models produced by the two fitting procedures were structurally aligned and averaged with the DAMAVER program. The resulting two average Hc structures were compared using the SUPCOMB spatial alignment program (from the DAMAVER suite), which gave a normalized spatial discrepancy (NSD) value of 0.63. NSD value is a quantitative

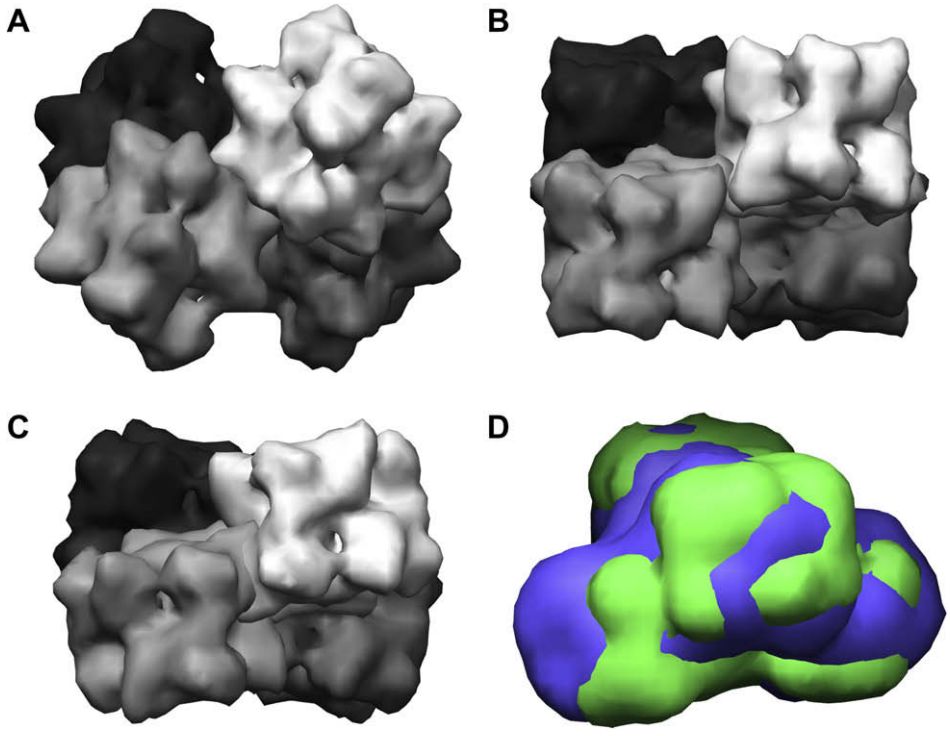

Fig. 4. Final models of *U. pusilla* Hc. Structures of the three symmetrical, representative *U. pusilla* best-fit models (1, 2 and 3) are shown in (A–C), respectively. (D) The superposition of the average symmetric (green) and asymmetric (blue) model structure, showing an overall common shape. (For interpretation of the references to colour in this figure legend, the reader is referred to the web version of this article.)

estimate of structural similarity between two aligned objects. When this value is smaller than one, the two objects can be considered equal (Kozin and Svergun, 2001). Fig. 4D shows the superposition of the averaged symmetrical and asymmetrical model showing their common overall shape.

In order to distinguish which one of the three symmetrical *U. pusilla* Hc models represents the actual protein structure, we have compared EM images of negatively stained proteins with SAXS derived models. SAXS models were converted to low-pass filtered volume densities and their 2D projections were calculated from 190 quasi-uniformly distributed orientations within the asymmetric triangle. A total 370 Hc particles extracted from EM micrographs were individually aligned to 570 projections of SAXS models. In this way 48.1% of EM particle images aligned to projections of SAXS model 2, 26.8% aligned to model 1 and 25.1% to model 3 (Supplementary Fig. 2). Fig. 5 shows the average of particles in one common orientation compared to its best model 2 volume projection.

4. Discussion

In this work we have used small angle X-ray scattering technique to characterize the structures of three arthropod Hcs in solution, presenting different levels of quaternary structure complexity. The use of this method in structural biology is encouraged due to the additional information obtainable from measurements in native-like solutions that can be hidden to EM and high-resolution crystallographic methods (Corbett et al., 2007). The first structure analyzed, the 2 × 6-meric Hc from *C. aestuarii*, was the easiest model to study since it shares the oligomeric structure with other crustacean Hcs whose structure has been thoroughly described: the crab *C. pagurus* (De Haas et al., 1991) and the lobster *H. americanus* (Hartmann et al., 2001). The analysis of *C. aestuarii* Hc SAXS data was important as a test set and development of modeling strategies used with the other two explored structures: the peculiar, stacked 2 × 6-meric Hc from the stomatopod *S. mantis* and the tetrahedral 4 × 6-meric structure from the thalassinid shrimp *U. pusilla*. The structures of these two unusual Hcs types are only partially described up to date (Bijlholt and van Bruggen, 1986; Cavellec et al., 1989).

Arthropod Hcs are composed of heterogeneous subunits and, out of the three investigated Hc species, only one subunit has been sequenced (*C. aestuarii* gamma-type subunit (Dolashka-Angelova and et al., 2005). Nevertheless arthropod Hcs share a high degree of sequence similarity ranging from 30% to 70% implying a conserved tertiary structure, which is easily observed from EM analysis (Markl and Decker, 1992; Burmester, 2002; Linzen and et al., 1985). This assumption was the basis for the use of the crystal structure of a different Hc to model all three crustacean Hcs, as previously done by other authors (Hartmann et al., 2001; Hartmann and Decker, 2002). To validate the use of the available crystal structures as building blocks for *Carcinus*, *Squilla* and *Upogebia* Hcs, we have compared the calculated SAXS patterns from *P. interruptus* and cheliceratan *L. polyphemus* Hcs (Hazes et al., 1993) against the experimental curve of *C. aestuarii* pH-stable hexamer (Dainese et al., 1998). Such hexamer is the only *C. aestuarii* structure that can be purified and maintained in solution without further aggregation to 2 × 6-mers. Sequence alignments show that higher identity exists between *C. aestuarii* versus *P. interruptus* (56%) as compared with *C. aestuarii* versus *L. polyphemus* (30%). In agreement, *P. interruptus* hexameric structure fitted significantly better the SAXS pattern of *C. aestuarii* pH-stable hexamer than the *L. polyphemus* structure (data not shown).

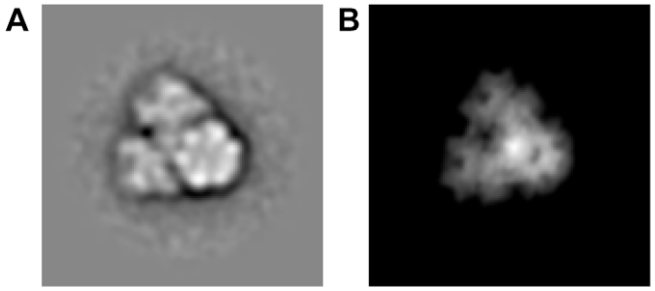

Fig. 5. Comparison of an EM view of *U. pusilla* Hc and SAXS best-fit model 2. (A) Example average of one class of negatively stained views of *U. pusilla* Hc particles. (B) Volume projection of model 2 *U. pusilla* Hc rotated and aligned to match the average EM view shown in (A).

C. aestuarii dodecameric Hc obtained from solution scattering data showed a typical cheliceratan oligomeric structure, with the threefold axes of the two stacked hexamers almost perpendicular to each other, while one of the twofold axes of each hexamer run parallel to the long axis of the structure (Fig. 6A with stereo views in Supplementary Fig. 3A). The interfaces between the two hexameric building blocks are less symmetrical than published data and seem to involve two subunits from the lower hexamer and three subunits from the upper one. From the low-resolution SAXS reconstruction we can estimate that the interacting subunits are mostly in contact through their first and third domains. In Fig. 6A, the inter-hexameric distance and the tilt angle between the two hexamers are shown to better visualize the structure of the best-fit model.

The Hc structure from *S. mantis* shows a peculiar inter-hexameric subunit arrangement and so far it represents a unique structure shared among stomatopod crustacea. Typical crustacean and cheliceratan 2 × 6-mers are arranged so that their hexameric building blocks are in contact through their short, rough sides. Instead stomatopod Hcs have their building blocks stacked on their long, flat sides as shown in Fig. 6B and Supplementary Fig. 3B, compared to Fig. 2. Negative-stain electron microscopy analysis described roughly the mutual position and overlap of the two building blocks and two different models were proposed differing in the orientation of the upper hexamer (called models I and III (Bijlholt and van Bruggen, 1986). In model I, one subunit from the lower hexamer interacts with one subunit from the upper one. Model III has both hexamers rotated by 60° showing two subunits from the lower hexamer in contact with two subunits from the upper one. Our best-fit SAXS model confirms the model III structure for *S. mantis* Hc although the upper hexamer had to be shifted by 13.6 Å closer to the lower one. Discrepancies of more than 1 nm in subunits positional placements between EM and solution scattering data have been previously reported (Hartmann et al., 2001; Decker et al., 1996) and are attributed to the use of negative staining. Besides simple translational optimization of the upper subunit, a full translational and rotational search was utilized to further increase the accuracy of the SAXS generated model. Comparing this solution structure of *S. mantis* Hc to all known 2 × 6-meric Hc aggregates, a structural analog can be found in the half molecule of Hc from *L. polyphemus* and other Chelicerata that show a 4 × 6-meric structure. Cheliceratan 4 × 6-meric Hcs are composed by the dimerization of a 2 × 6-mer (called dodecamer) in an antiparallel orientation (Martin and et al., 2007; Cong and et al., 2009). This 2 × 6-mer is highlighted in the *P. imperator* Hc structure shown in red and yellow colors in Fig. 6D. However, another structurally different 2 × 6-mer can be singled out taking into account adjacent hexamers from each dodecamer of the native 4 × 6-mer. In Fig. 6D, the structure of this 2 × 6-mer is highlighted in red and blue. This alternative 2 × 6-mer presents high structural homology to *S. mantis* Hc besides the handedness since both enantiomers produce the same scattering pattern. The inter-hexameric

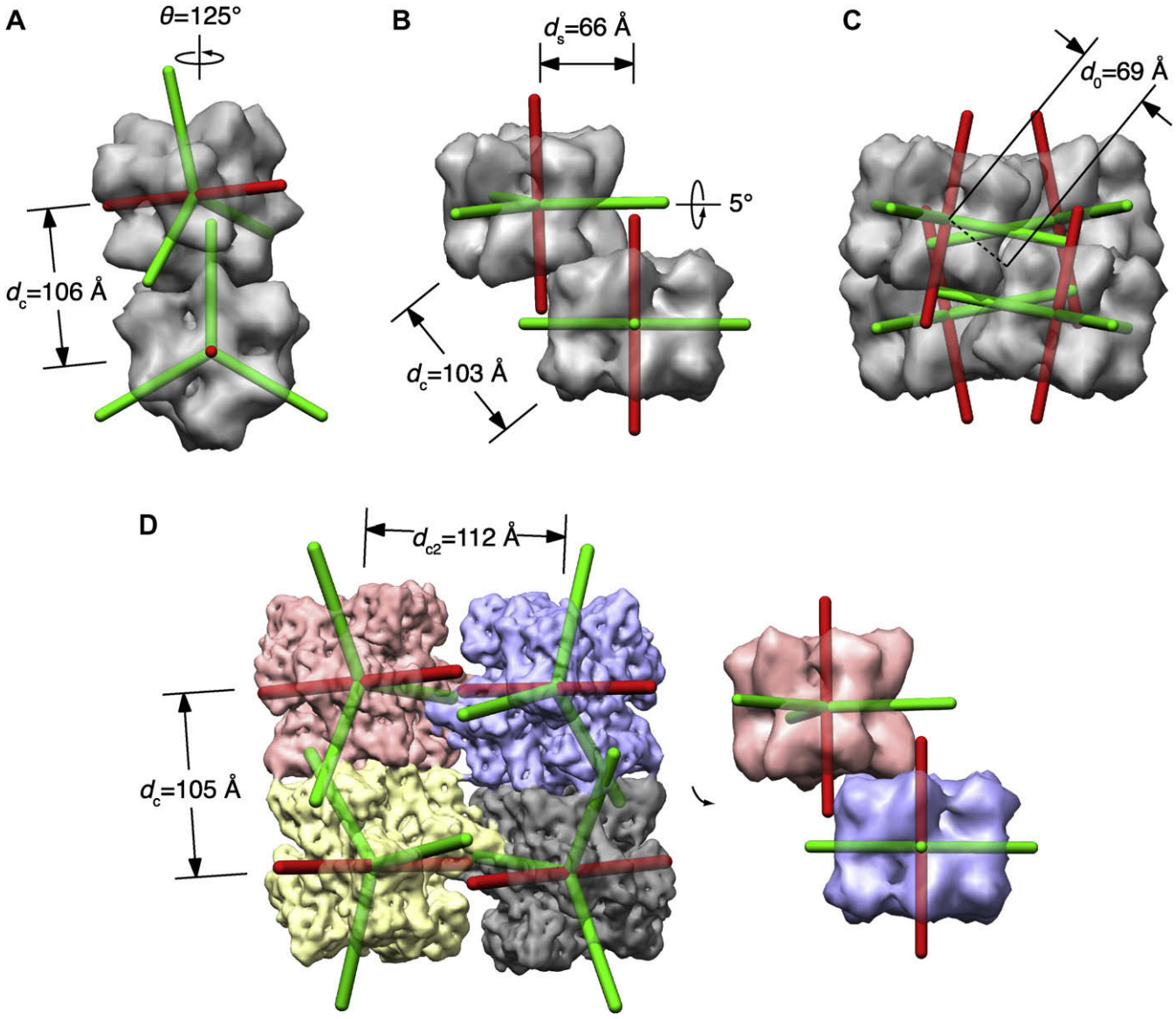

Fig. 6. Structural parameters and geometries of SAXS best-fit models. Top row shows structural parameters and geometries of final, SAXS best-fit models of the three investigated Hcs, namely *C. aestuarii* (A), *S. mantis* (B) and *U. pusilla* Hc (C). For stereo views of the same models see Supplementary Fig. 3. *U. pusilla* Hc is shown rotated by 90° around the vertical axis with respect to the view in Fig 4B. Panel (D) shows the Cryo-EM model of *P. imperator* 4 × 6-meric Hc with the extracted 2 × 6-mer used as starting model for *S. mantis* Hc (see Fig. 3C). Colors indicate individual hexamers: red and yellow ones represent the dodecamer or the building block for 4 × 6 and 8 × 6-meric Hcs while red and blue ones represent the 2 × 6-mer similar to *S. mantis* Hc. In all panels, red cylinders show the trimeric axis and green ones show three dimeric symmetry axes of the D_3 hexameric building block, as an aid to visualize mutual subunit orientations. d_c and d_{c2} are the distances between the center of mass of the two alternative 2 × 6-mers; d_0 is the distance from the hexamers centers to the molecule center; d_s represents the shift of the upper subunit and is calculated as the projection of the inter-hexameric distance on the plane spanned by lower hexamer twofold axes and θ is the relative rotation between the two hexamers around the inter-hexameric axis. Note that inter-hexameric distance d_c in *S. mantis* Hc corresponds topologically to the distance d_{c2} in 4 × 6-meric/8 × 6-meric Hcs. (For interpretation of the references to color in this figure legend, the reader is referred to the web version of this article.)

distance in the modeled *S. mantis* Hc is much shorter than those found in cheliceratan 4 × 6-meric (~103 Å versus 107–112 Å) (Fig. 6 and Table 3). That could be due to inter-hexameric contacts in *S. mantis* being the only, and therefore most important interface in the molecule. On the other hand, in cheliceratan structures the major interface is among the hexamers in the dodecamer, while interdodecameric contacts are mostly involved in conformational changes due to allosteric effectors (Cong and et al., 2009).

The final best-fit structure has the geometry similar as the EM-derived model III, with two subunits in contact with other two from the lower hexamer. Mutual inter-hexameric orientation is not as symmetrical as model III suggested. As visualized in Fig. 6B, the two hexamers are not simply stacked one on the other and shifted by 66 Å but their threefold axes are rotated by 5°. As a consequence, the tilt of the upper hexamer produces asymmetrical inter-hexameric contacts among the four involved subunits.

As much as *S. mantis* Hc differs from all other 2 × 6-meric Hcs, so does the *U. pusilla* among 4 × 6-meric ones. Average low-resolution SAXS based models of *U. pusilla* were obtained assuming a symmetrical (D_2) and asymmetrical (C_1) arrangement of hexameric building blocks. The two structures showed an overall similar shape with comparable goodness of the fit values. Therefore, at this resolution, we have no evidence to prefer a more complex (asymmetrical) model as the correct one for the *U. pusilla* Hc. In order to increase the resolution of the structure, we have clustered and averaged all generated symmetrical models. The models converged

Table 3
Comparison of structural parameters of modeled hemocyanins.

Hemocyanin	Method	Structural parameters[a]			Reference
		d_c distance [Å]	θ rotation [°]	d_{c2} distance [Å]	
4 × 6-meric *E. californicum* (oxy)	SAXS	105.1 ± 1.3	105 ± 7	107.4 ± 1.4	Hartmann and Decker (2002)
4 × 6-meric *E. californicum* (deoxy)	SAXS	104.5 ± 0.8	131 ± 3	103.7 ± 0.8	Hartmann and Decker (2002)
4 × 6-meric *P. imperator* (resting state)	3D-EM	105 ± 1	101 ± 1	112 ± 1	Cong and et al. (2009)
8 × 6-meric *L. polyphemus* (half molecule)	3D-EM	100 ± 3	105 ± 5	111 ± 3	Martin and et al. (2007)
2 × 6-meric *C. magister*, *H. americanus* (oxy)	3D-EM, SAXS	108 ± 1	101 ± 1	–	Hartmann et al. (2001), De Haas et al. (1991)
2 × 6-meric *C. aestuarii* (oxy)	SAXS	106 ± 1	125 ± 5	–	This work
		d_c distance [Å][b]	d_s distance [Å]		
2 × 6-meric *S. mantis* (model III)	2D-EM	110 ± 20	50 ± 20		Bijlholt and van Bruggen (1986)
2 × 6-meric *S. mantis* (oxy)	SAXS	102.9 ± 0.5	66.2 ± 0.5		This work
		d_0 distance [Å]			
4 × 6-meric *U. pusilla* (oxy)	SAXS	69 ± 5			This work

[a] Structural parameters are the same as in Fig. 6: d_c and d_{c2} are the distances between the center of mass of the two alternative 2 × 6-mers; d_0 is the distance from the hexamers centers to the molecule center; d_s represents the shift of the upper subunit and is calculated as the projection of the inter-hexameric distance on the plane spanned by lower hexamer twofold axes; θ is the relative rotation between the two hexamers around the inter-hexameric axis.
[b] The inter-hexameric distance d_c in *S. mantis* hemocyanin corresponds topologically to the distance d_{c2} in 4 × 6-meric/8 × 6-meric hemocyanins.

to three distinct structural solutions but equivalent from the SAXS point of view. By comparing the structural solutions with negative-stain EM micrographs of *U. pusilla* Hc we are able to discern the most probable structural model among the three proposed. Although negative-stain EM is typically limited to 20 Å resolution, the precision of positional information when utilizing a hybrid approach (EM and crystallographic techniques) is around 5 Å (van Heel and Dube, 1994), thus validating our method. Majority of boxed EM particles were most similar to the simulated two-dimensional projections of only one SAXS based structural model (model 2). In model 2, four hexameric building blocks are in contact with each other, each contributing mainly with only one subunit (Fig. 6C with stereo views in Supplementary Fig. 3C).

As far as the precision of the generated models is concerned, some general considerations could be put forward. SAXS based rigid body modeling with utilized programs is a stochastic process and therefore can produce sub-optimal models. In order to obtain the most accurate reconstruction from analyzed proteins, two main precautions were taken: first, we have used different starting models where applicable (*E. californicum* and *C. pagurus* for *C. aestuarii* Hc and two negative-stain EM-derived models and *P. imperator* for *S. mantis* Hc). Initial *C. aestuarii* models were tried also on *S. mantis* and *U. pusilla* Hcs but produced incorrect results. Second, the minimization process was guided using large angular and spatial step sizes followed by smaller ones in order to effectively sample the parameter space. The finest step sizes utilized in the modeling process limit the resolution of the reconstructions and are 1 Å and 5° for *C. aestuarii*, 0.5 Å and 2° for *S. mantis* and 5 Å and 20° for *U. pusilla* models. We estimated the error of the final models in the following way: for every final model, we have constructed all neighboring structures in six-dimensional parameter space offset by the finest step size used in the reconstruction (in total $3^6 - 1 = 728$ models). Successively, scattering curves of all 728 models were calculated and averaged. Standard deviation of the averaged scattering intensities was used as an approximation of model errors (Supplementary Fig. 4). It is clear that for small step sizes (<1 Å/5°), neighboring models produce almost identical scattering patterns so a more realistic estimate of the actual resolution lies in the range of 1–5 Å for translational parameters and 5–20° for angular parameters.

5. Conclusions

Arthropod Hcs represent a structurally heterogeneous class of oxygen transport proteins whose presence (and absence) in various *taxa* is still poorly understood and fails to be predicted from evolutionary relationships and animal behavior alone. In order to gain insight into this complex group of proteins, two approaches are currently ongoing. On one hand, the subunit heterogeneity of Hc is investigated at biochemical and molecular level starting with subunit identification and separation (with immunological and biophysical methods) and ending with complete sequencing of all subunit types present in native proteins. On the other hand, a structural approach, mainly coming form X-ray solution scattering and (cryo-)EM data analysis, gave insight into a native-like oligomeric assembly followed by higher resolution analyses showing conformational changes and functional modulation of these giant proteins.

In order to increase the structural coverage of known oligomeric states of arthropod Hcs, we have determined the solution structures of two unusual Hc oligomers, a 2 × 6-meric one from *S. mantis* and a 4 × 6-meric one from *U. pusilla*. In addition, a 2 × 6-meric Hc from *C. aestuarii* was determined as a representative, characteristic structure. With the term unusual we intend a quaternary structure found in an isolated, small clade and showing no structural homologs among other arthropod *taxa*. Small angle X-ray scattering allowed us to describe the low-resolution structure of *U. pusilla* Hc with its symmetrical, tetrahedral subunit arrangement as compared to the more common square planar structure found within Chelicerata. The reconstructed structure of 2 × 6-meric *S. mantis* Hc showed a subunit arrangement that resembles a substructure found in cheliceratan 4 × 6-meric and 8 × 6-meric Hcs. Higher resolution structures and sequencing information are needed to clarify if it is the case of structural convergence or homology.

Small angle scattering has proven as an excellent tool in structural biology, although at low resolution, but with the possibility of operation in unperturbed, native-like conditions. This method can complement quite well high-resolution electron microscopy, with the ability to improve on some EM-derived models, and on the other hand, utilize image analysis to discriminate and validate ambiguous solutions. It is becoming clear that structural data alone are insufficient to fully understand the relationships and distributions of Hc structures within Arthropods. The integration of full subunit sequences together with the mapping of various subunit types to low or medium resolution native structures are the key to thoroughly describe the structure–function relationships in this vast group of giant oxygen carriers.

Acknowledgments

We thank Prof. Heinz Decker (University of Mainz) for helpful discussion on modeling strategy, Prof. Silvio Tosatto (University

of Padova) for providing access to his Linux cluster and Theyencheri Narayanan and the staff of ID2 beamline at the ESRF (Grenoble) for assistance during measurements. This work was supported by a "Progetto di Ateneo" Grant CPDA 051777 from the University of Padova and the Grant CLODIA from Regione Veneto (M.B.). I.M. acknowledges a postdoctoral fellowship from the University of Padova.

Appendix A. Supplementary data

Supplementary data associated with this article can be found, in the online version, at doi:10.1016/j.jsb.2010.03.012.

References

Bijlholt, M., van Bruggen, E., 1986. A model for the architecture of the hemocyanin from the arthropod *Squilla mantis* (Crustacea, Stomatopoda). Eur. J. Biochem. 155, 339–344.

Bijlholt, M., van Heel, M., van Bruggen, M., 1982. Comparison of 4×6-meric hemocyanins from three different arthropods using computer alignment and correspondence analysis. J. Mol. Biol. 161, 139–153.

Bruneaux, M., Terrier, P., Leize, E., Mary, J., Lallier, F., Zal, F., 2009. Structural study of *Carcinus maenas* hemocyanin by native ESI-MS: interaction with L-lactate and divalent cations. Proteins 77, 589–601.

Bubacco, L., Magliozzo, R.S., Beltramini, M., Salvato, B., Peisach, J., 1992. Preparation and spectroscopic characterization of a coupled binuclear center in cobalt(II)-substituted hemocyanin. Biochemistry 31, 9294–9303.

Burmester, T., 2002. Origin and evolution of arthropod hemocyanins and related proteins. J. Comp. Physiol. B. 172, 95–107.

Cavellec, A., Boisset, N., Taveau, J.C., Lamy, J.N., 1989. Image processing of electron-microscopic views of *Callianassa californiensis* hemocyanin. In: Préaux, G., Lontie, R. (Eds.), Invertebrate Dioxygen Carriers. Leuven University Press, Louvain, pp. 271–274.

Cong, Y. et al., 2009. Structural mechanism of SDS-induced enzyme activity of scorpion hemocyanin revealed by electron cryomicroscopy. Structure 17, 749–758.

Corbett, K.D., Benedetti, P., Berger, J.M., 2007. Holoenzyme assembly and ATP-mediated conformational dynamics of topoisomerase VI. Nat. Struct. Mol. Biol. 14, 611–619.

Dainese, E., Di Muro, P., Beltramini, M., Salvato, B., Decker, H., 1998. Subunits composition and allosteric control in *Carcinus aestuarii* hemocyanin. Eur. J. Biochem. 256, 350–358.

De Haas, F., van Bruggen, E., 1994. The interhexameric contacts in the four-hexameric hemocyanin from the tarantula *Eurypelma californicum*. A tentative mechanism for cooperative behavior. J. Mol. Biol. 237, 464–478.

De Haas, F., Bijlholt, M., van Bruggen, E., 1991. An electron microscopic study of two-hexameric hemocyanins from the crab *Cancer pagurus* and the tarantula *Eurypelma californicum*: determination of their quaternary structure using image processing and simulation models based on X-ray diffraction data. J. Struct. Biol. 107, 86–94.

Decker, H., Savel-Niemann, A., Körschenhausen, D., Eckerskorn, E., Markl, J., 1989. Allosteric oxygen-binding properties of reassembled tarantula (*Eurypelma californicum*) hemocyanin with incorporated apo- or met-subunits. Biol. Chem. Hoppe Seyler 370, 511–523.

Decker, H., Hartmann, H., Sterner, R., Schwarz, E., Pilz, I., 1996. Small-angle X-ray scattering reveals differences between the quaternary structures of oxygenated and deoxygenated tarantula hemocyanin. FEBS Lett. 393, 226–230.

Dolashka-Angelova, P. et al., 2005. Structure of hemocyanin subunit CaeSS2 of the crustacean Mediterranean crab *Carcinus aestuarii*. J. Biochem. 138, 303–312.

Frank, J., Radermacher, M., Penczek, P.A., Zhu, J., Li, Y., Ladjadj, M., Leith, A., 1996. SPIDER and WEB: processing and visualization of images in 3D electron microscopy and related fields. J. Struct. Biol. 116, 190–199.

Hartmann, H., Decker, H., 2002. All hierarchical levels are involved in conformational transitions of the 4×6-meric tarantula hemocyanin upon oxygenation. Biochim. Biophys. Acta 1601, 132–137.

Hartmann, H., Decker, H., 2004. Small-angle scattering techniques for analyzing conformational transitions in hemocyanins. Methods Enzymol. 379, 81–106.

Hartmann, H., Lohkamp, B., Hellmann, N., Decker, H., 2001. The allosteric effector l-lactate induces a conformational change of 2×6-meric lobster hemocyanin in the oxy state as revealed by small angle x-ray scattering. J. Biol. Chem. 276, 19954–19958.

Hazes, B., Magnus, K.A., Bonaventura, C., Bonaventura, J., Dauter, Z., Kalk, K.H., Hol, W.G., 1993. Crystal structure of deoxygenated *Limulus polyphemus* subunit II hemocyanin at 2.18 Å resolution: clues for a mechanism for allosteric regulation. Protein Sci. 2, 597–619.

Kozin, M., Svergun, D.I., 2001. Automated matching of high- and low-resolution structural models. J. Appl. Crystallogr. 34, 33–41.

Kusche, K., Hembach, A., Hagner-Holler, S., Gebauer, W., Burmester, T., 2003. Complete subunit sequences, structure and evolution of the 6×6-mer hemocyanin from the common house centipede, *Scutigera coleoptrata*. Eur. J. Biochem. 270, 2860–2868.

Li, Y., Wang, Y., Jiang, H., Deng, J., 2009. Crystal structure of *Manduca sexta* prophenoloxidase provides insights into the mechanism of type 3 copper enzymes. Proc. Natl Acad. Sci. USA 106, 17002–17006.

Linzen, B. et al., 1985. The structure of arthropod hemocyanins. Science 229, 519–524.

Ludtke, S.J., Baldwin, P.R., Chiu, W., 1999. EMAN: semiautomated software for high-resolution single-particle reconstructions. J. Struct. Biol. 128, 82–97.

Magnus, K.A., Hazes, B., Ton-That, H., Bonaventura, C., Bonaventura, J., Hol, W.G., 1994. Crystallographic analysis of oxygenated and deoxygenated states of arthropod hemocyanin shows unusual differences. Proteins 19, 302–309.

Markl, J., Decker, H., 1992. Molecular structure of the arthropod hemocyanins. In: Mangum, C.P. (Ed.), Advances in Comparative and Environmental Physiology. Springer-Verlag, Berlin Heidelberg, pp. 325–376.

Markl, J., Moeller, A., Martin, A., Rheinbay, J., Gebauer, W., Depoix, F., 2009. Ten-Angstrom CryoEM structure and molecular model of the myriapod (*Scutigera*) 6×6mer hemocyanin: understanding a giant oxygen transport protein. J. Mol. Biol 392, 362–380.

Martin, A.G. et al., 2007. *Limulus polyphemus* hemocyanin: 10 Å cryo-EM structure, sequence analysis, molecular modelling and rigid-body fitting reveal the interfaces between the eight hexamers. J. Mol. Biol. 366, 1332–1350.

Meissner, U., Stohr, M., Kusche, K., Burmester, T., Stark, H., Harris, R., Orlova, E.V., Markl, J., 2003. Quaternary structure of the European spiny lobster (*Palinurus elephas*) 1×6-mer hemocyanin from cryoEM and amino acid sequence data. J. Mol. Biol. 325, 99–109.

Narayanan, T., Diat, O., Bösecke, P., 2001. SAXS and USAXS on the high brilliance beamline at the ESRF. Nucl. Instrum. Methods A 467, 1005–1009.

Ohi, M., Li, Y., Cheng, Y., Walz, T., 2004. Negative staining and image classification – powerful tools in modern electron microscopy. Biol. Proced. Online 6, 23–34.

Paoli, M., Giomi, F., Hellmann, N., Jaenicke, E., Di Muro, P., Beltramini, M., 2007. The molecular heterogeneity of hemocyanin: Structural and functional properties of the 4×6-meric protein of *Upogebia pusilla* (Crustacea). Gene 398, 177–182.

Petoukhov, M.V., Svergun, D.I., 2005. Global rigid body modeling of macromolecular complexes against small-angle scattering data. Biophys. J. 89, 1237–1250.

Salvato, B., Beltramini, M., 1990. Hemocyanins: molecular architecture, structure and reactivity of the binuclear copper active site. Life Chem. Rep. 8, 1–47.

Svergun, D.I., 1992. Determination of the regularization parameter in indirect-transform methods using perceptual criteria. J. Appl. Crystallogr. 25, 495–503.

Svergun, D.I., Semenyuk, A., Feigin, L., 1988. Small-angle-scattering-data treatment by the regularization method. Acta Crystallogr. A 44, 244–250.

Svergun, D.I., Barberato, C., Koch, M.H.J., 1995. CRYSOL – a program to evaluate x-ray solution scattering of biological macromolecules from atomic coordinates. J. Appl. Crystallogr. 28, 768–773.

Taveau, J.C., Boisset, N., Lamy, J., Lambert, O., Lamy, J.N., 1997. Three-dimensional reconstruction of *Limulus polyphemus* hemocyanin from cryoelectron microscopy. J. Mol. Biol. 266, 1002–1015.

van Heel, M., Dube, P., 1994. Quaternary structure of multihexameric arthropod hemocyanins. Micron 25, 387–418.

Voit, R., Feldmaier-Fuchs, G., Schweikardt, T., Decker, H., Burmester, T., 2000. Complete sequence of the 24-mer hemocyanin of the tarantula *Eurypelma californicum*. Structure and intramolecular evolution of the subunits. J. Biol. Chem. 275, 39339–39344.

Volbeda, A., Hol, W.G., 1989. Crystal structure of hexameric haemocyanin from *Panulirus interruptus* refined at 3.2 Å resolution. J. Mol. Biol. 209, 249–279.

Volkov, V.V., Svergun, D.I., 2003. Uniqueness of ab initio shape determination in small-angle scattering. J. Appl. Crystallogr. 36, 860–864.

Wriggers, W., Chacon, P., 2001. Using situs for the registration of protein structures with low-resolution bead models from X-ray solution scattering. J. Appl. Crystallogr. 34, 773–776.